Hindawi
Mathematical Problems in Engineering
Volume 2022, Article ID 9082752, 17 pages
https://doi.org/10.1155/2022/9082752

Research Article

Design and Analysis of a Novel Quasi-Zero Stiffness Isolator under Variable Loads

Yingjiang Xie, Fu Niu, Jinggong Sun, and Lingshuai Meng

Academy of Systems Engineering, Academy of Military Sciences, Beijing 100166, China

Correspondence should be addressed to Jinggong Sun; sunjggg@163.com and Lingshuai Meng; mengls1989@sina.com

Received 28 July 2021; Accepted 24 December 2021; Published 31 January 2022

Academic Editor: Agathoklis Giaralis

The designed load of most quasi-zero stiffness (QZS) isolators is constant. The isolation performance will drop sharply once the load changes. A novel QZS isolator that can adapt to variable loads is proposed in this paper to improve the range of application of the isolator. The isolator is designed by paralleling the electromagnetic spring (ES), which provides negative stiffness, and the pneumatic spring (PS), which provides positive stiffness. The positive and negative stiffness can be adjusted by changing the pressure and coil current, which provides the possibility for the isolator to adapt to variable loads. This paper derived the conditions for the isolation system to obtain QZS characteristics, proposed the dynamic model of the isolation system, derived and verified the analytical expressions of the amplitude-frequency response and force transmissibility (FT), and discussed the change of FT and displacement transmissibility(DT) under different loads. Theoretical analysis shows that changing the pressure and coil current in the same proportion can maintain the superior low-frequency isolation performance when the load changes, thanks to the preservation of the QZS characteristics of the system after adjusting the pressure and coil current. Finally, the simulation results fg and isolation frequency band over the linear isolation system and PS isolation system. Furthermore, the proposed isolator can be adjusted online.

1. Introduction

Vibration is pervasive in the engineering field, and various instruments and equipment are constantly disturbed by vibration from the base or other dynamic loads. At present, linear vibration isolators are widely used in aerospace, vehicles, and other engineering fields to reduce vibration harm. However, the linear isolator only works in the range of more than $\sqrt{2}$ times the natural frequency of the system according to the vibration theory. The only way to broaden the isolation frequency band is to reduce the stiffness of the system, which will result in poor static supportability and system stability. Therefore, some novel isolation systems have been continuously developed and upgraded to solve these inherent contradictions, such as the isolator with inerter-based damper and the quasi-zero stiffness (QZS) isolator. The inerter has a negative stiffness effect, which can be used to reduce the natural frequency of the system [1]. Nakamura et al. [2] proposed an electromagnetic inertial mass damper (EIMD) composed of a ball screw and a generator, and the shaking table test results verified the vibration control performance of the structure. Then, Wang et al. [3] carried out simulation experiments on a five-story building using seismic records and the results show that the EIMD can significantly improve the seismic performance of the base-isolated structure. Reference [4] verified that the base-isolated structure with attached tuned mass damper inerter has a smaller displacement peak by carrying out a shaking table test. However, the negative stiffness generated by inerter increases with the increase of external frequency, so it is difficult to coordinate low-frequency isolation performance and high-frequency response [5]. The QZS isolator composed of positive and negative stiffness mechanisms has drawn much attention of researchers due to the high static support capacity and low dynamic stiffness, which can overcome the above-mentioned shortcomings.

There are many methods to obtain QZS, and a typical way is combining two oblique springs with vertical springs

in parallel [6–10]. Gatti [11] arranged four linear springs inclined and symmetrically for vibration isolation. Inspired by the structure of the bionic limb, Zhao et al. [12] combined three pairs of oblique springs with vertical springs in parallel to form a novel QZS isolator. Subsequently, the cam-roller-spring mechanism [13–15] was further studied. Recently, Wang et al. [16, 17] combined the diamond-shaped negative stiffness structure and inertial dampers to design a new type of inertial-based QZS isolator, which has good nonlinear stiffness characteristics and mass amplification effects and can achieve superior vibration isolation performance. In the past decade, magnets have gradually become the focus of research topics due to their noncontact and nonfriction characteristics [18–21]. Furthermore, the coil winding is used instead of the magnet to improve the controllability of the isolator [22–25]. Liu et al. [26] formed a new nonlinear isolator by arranging the electromagnetic spring (ES) symmetrically on both sides of the central axis of the vertical linear spring, which can realize QZS with the appropriate current. Yuan et al. [27] combined a linear ES with a linear spring in parallel to form a new type of QZS isolator, which can be adjusted online under large excitation. Pu et al. [28] arranged the coaxial coils and magnets in multiple layers to expand the adjustable area of negative stiffness. Jiang et al. [29] obtained a good isolation effect by connecting the air spring and ES in parallel. In addition, other structures such as a circular ring [30], disc springs [31], a rope structure [32], flexible rods [33], and an X-shaped structure [34] can also obtain QZS characteristics.

For most QZS isolators, the new equilibrium position of the isolation system will deviate from the set working position once the load changes, and the stiffness of the system will no longer be close to zero, which causes the isolation performance to drop sharply. This paper proposes a novel QZS isolator composed of the pneumatic spring (PS) and ES that can adapt to different loads to solve the problem. The isolator has high static support capacity and near-zero dynamic stiffness when pressure and coil current are applied. Similarly, the isolation system can maintain the QZS characteristics under different loads by adjusting the pressure and current of the isolator.

2. Model of the QZS Isolator

The QZS isolator composed of load, ES element, PS element, and base is shown in Figure 1(a), where the ES is symmetrically arranged on both sides of the central axis of the PS. In addition, the isolator also includes sleeves, compression nuts, guide posts, connecting rods, stud bolts, connectors, and other components.

The ES element is the negative stiffness mechanism of the QZS isolation system, which comprises a pair of coil windings and a ring magnet arranged coaxially. The coil winding and the ring magnet are attracted to each other when the current is applied to the coil winding, which thereby generates the required negative stiffness. The coil windings are fixed by a compression nut. The ring magnets on both sides are connected by a stud bolt to ensure that their movements are synchronous. The coil winding and the ring magnet are installed in the sleeve, and the ring magnet can slide vertically in the sleeve. The PS element is the positive stiffness mechanism of the isolation system, which is composed of a cylinder with two chambers and a piston rod and is used to support the load. Both ES and PS are fixed on the base. The connector connects the ES, the PS, and the load to ensure that the ring magnet, the piston rod, and the load have the same movement.

The traditional QZS isolator is mainly composed of a linear spring and a nonlinear negative stiffness mechanism, and the stiffness is difficult to adjust. It can be known from Section 3 that the electromagnetic force of ES and the restoring force of PS have nonlinear characteristics, and the negative stiffness produced by the ES and the positive stiffness produced by the PS can be controlled by adjusting the coil current and pressure. Therefore, the parallel combination of ES and PS can not only achieve QZS to reduce the natural frequency of the system and reduce the effects of external vibration on the isolated object but also maintain the nonlinear characteristics. The current direction of the coil winding and the magnetizing direction of the ring magnet are shown in Figure 1(b). The isolation system can be equivalent to a single degree of freedom (SDOF) system in the vertical direction due to the ring magnet and the piston rod only moving along the vertical direction. The equivalent model is shown in Figure 1(c).

3. Statics Analysis of the QZS Isolator

3.1. Calculation of the Electromagnetic Force and PS Restoring Force. The filament method [35] is applied in this study to calculate the attractive force generated by the energized coil winding and the ring magnet. The principle of this method is to regard the magnet and the energized coil windings as multiple Maxwell loop currents, calculate the attractive force between any pair of loop currents, and finally superimpose and sum the attractive forces to get the electromagnetic force of the ES. The calculation process of the filament method has been described in detail in References [26, 27], so it is omitted here. The electromagnetic force generated by the *ES* is given by

$$F_{ES} = F_{CM} + F_{DM}, \tag{1}$$

where F_{DM} and F_{CM} represent the attractive force produced by the ring magnet and the upper and lower energized coil windings, and the specific expression is given in Appendix.

The expression of negative electromagnetic stiffness is obtained by differentiating Equation (1) as follows:

$$K_{ES} = \frac{dF_{ES}}{dx}. \tag{2}$$

The calculation method of electromagnetic force mentioned above requires the elliptic integral, which will lead to complicated calculations. A polynomial fitting approximation is used for Equation (1) to make the result more intuitive and simplify the calculation. The approximate expression is as follows:

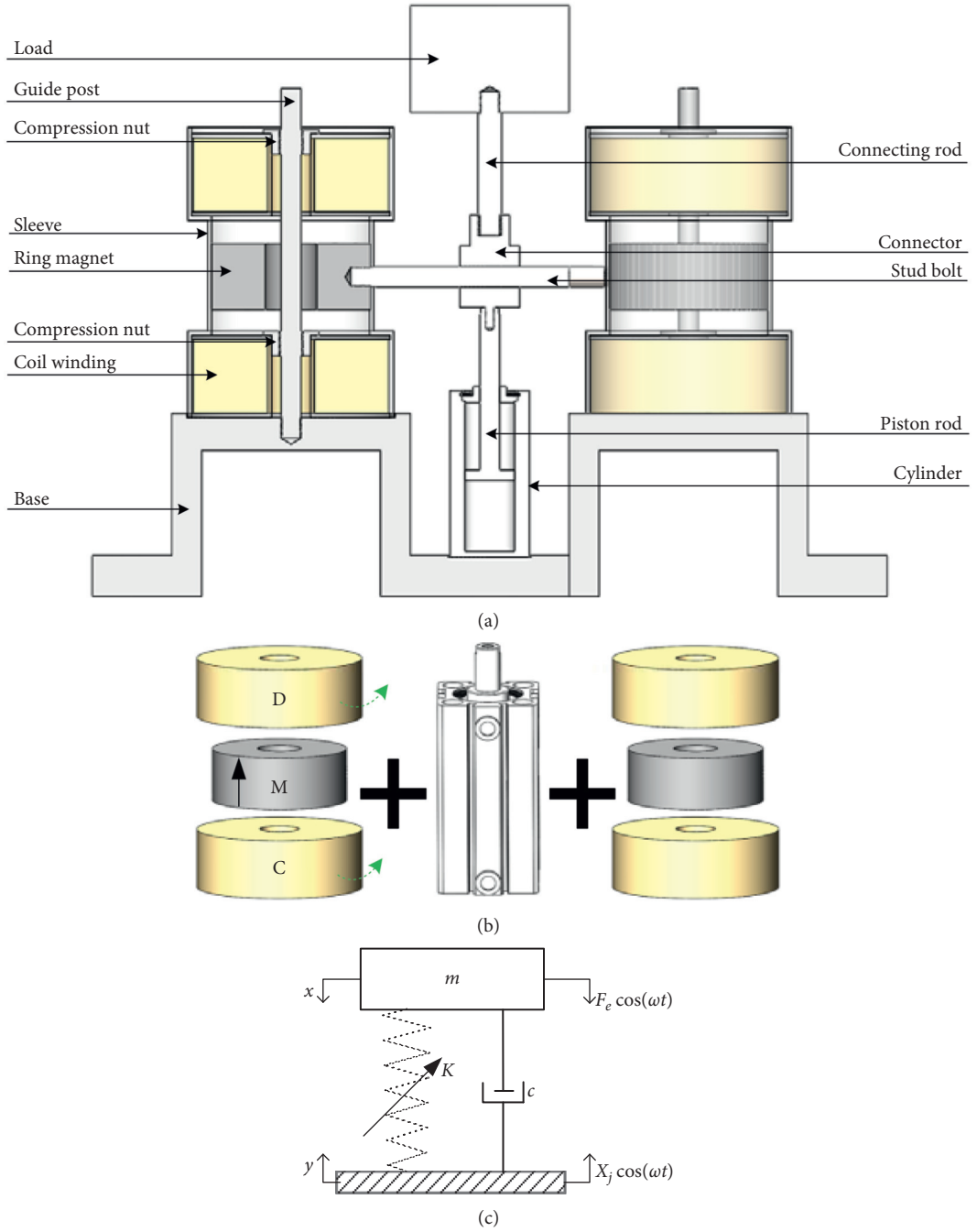

Figure 1: The QZS isolator. (a) Structural model (partial section view); (b) ES and PS; and (c) equivalent model of the isolator.

$$F_{ES} = \left(ax^3 + bx\right)i, \tag{3}$$

where a and b are the fitting parameters, i is the coil current, and x is the magnet displacement.

Figure 2 shows the electromagnetic force calculated by the filament method and the polynomial fitting results. The parameters involved are listed in Table 1.

The principle of the PS is to use the pressure difference between the upper and lower chambers to support the load. The restoring force of the PS when the pressure is applied is given by

$$F_p = p_l A_l \left(\frac{h_l}{h_l - x}\right)^{\lambda} - p_u A_u \left(\frac{h_u}{h_u + x}\right)^{\lambda}, \tag{4}$$

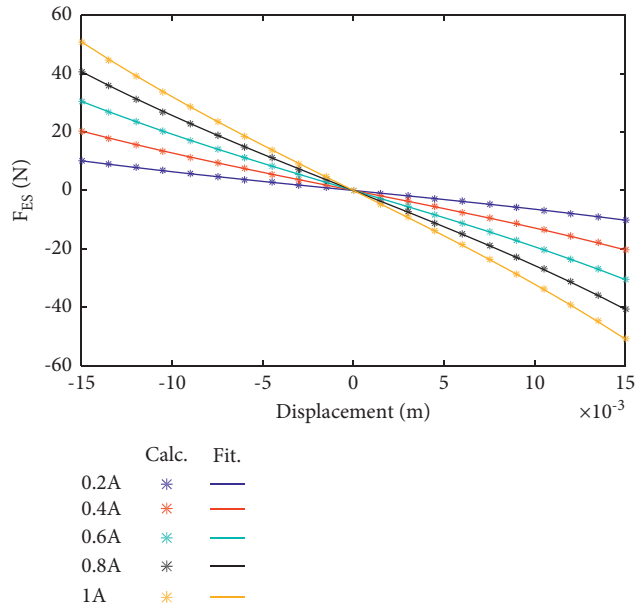

Figure 2: Calculated electromagnetic force and fitting results under different currents.

where p_u and p_l are the pressures of the upper and lower chambers, and the definitions and values of other parameters in Equation (4) are shown in Table 2.

3.2. Realization of the QZS Isolation System. The QZS isolator is obtained by paralleling the ES and PS. The restoring force of the isolation system when the isolator bears the load mg can be written as

$$F_{QZS} = p_l A_l \left(\frac{h_l}{h_l - x}\right)^{\lambda} - p_u A_u \left(\frac{h_u}{h_u + x}\right)^{\lambda} + 2\left(ax^3 + bx\right)i - mg. \tag{5}$$

Then, the stiffness and the first derivative of the stiffness of the isolation system are, respectively, as follows:

$$\begin{aligned} K_{QZS} &= \frac{dF_{QZS}}{dx} = p_l A_l \lambda {h_l}^{\lambda} \frac{1}{(h_l - x)^{\lambda+1}} + p_u A_u \lambda {h_u}^{\lambda} \frac{1}{(h_u + x)^{\lambda+1}} + 2\left(3ax^2 + b\right)i, \\ K'_{QZS} &= p_l A_l \lambda {h_l}^{\lambda} (\lambda + 1) \frac{1}{(h_l - x)^{\lambda+2}} - p_u A_u \lambda {h_u}^{\lambda} (\lambda + 1) \frac{1}{(h_u + x)^{\lambda+2}} + 2 \times 6axi. \end{aligned} \tag{6}$$

The position of the system in a stable state is set as the working position of the isolator, that is, $x = 0$. The distances between the ring magnet and the upper and lower coil windings are equal at this time; thus, the electromagnetic force is zero and the load is completely borne by the PS, which can be written as

$$p_l A_l - p_u A_u = mg. \tag{7}$$

The stiffness of the isolation system is zero at the working position of the isolator, and the following equation can be obtained:

$$K_{QZS} = p_l A_l \lambda \frac{1}{h_l} + p_u A_u \lambda \frac{1}{h_u} + 2bi = 0. \tag{8}$$

The first derivative of the stiffness is set to zero to make that the minimum stiffness of the isolation system in a balanced state is zero; thus, it can be written as follows:

$$K'_{QZS} = p_l A_l \lambda (\lambda + 1) \frac{1}{{h_l}^2} - p_u A_u \lambda (\lambda + 1) \frac{1}{{h_u}^2} = 0. \tag{9}$$

The QZS condition of the isolation system can be obtained from Equations (7)–(9) as follows:

$$p_l = \frac{mg}{A_l\left(1 - {h_u}^2/{h_l}^2\right)}, p_u = \frac{mg}{A_u\left({h_l}^2/{h_u}^2 - 1\right)}, i = -\frac{1}{2b} mg \left(\frac{\lambda}{h_l - h_u}\right). \tag{10}$$

The pressure and coil current are selected by Equation (10) once the load is determined, and the system can obtain the QZS characteristics.

It can be seen from Equation (10) that the pressure and coil current to achieve QZS characteristics are related to the height of the upper and lower chambers; thus, the design and selection of the height of the chamber are essential for the isolation system. Figure 3 shows the change of the force-displacement curve and the stiffness-displacement curve of

Table 1: Parameters of the *ES*.

Parameter	Unit	Value	Definition
R_{1C}	mm	11.8	The inner radius of the coil winding
R_{2C}	mm	49.2	The outer radius of the coil winding
R_{1M}	mm	13	The inner radius of the ring magnet
R_{2M}	mm	40	The outer radius of the ring magnet
H_C	mm	36	Height of the coil winding
H_M	mm	32	Height of the ring magnet
z	mm	15	Distance between ring magnet and coil winding
J	T	1.35	Magnetization of the ring magnet
N_{RC}	—	55	The number of radial turns of the coil winding
N_{HC}	—	50	The number of axial turns of the coil winding
N_{HM}	—	80	The number of axial turns of the ring magnet
N	—	2750	Turns of the coil winding
$i(C)$	A	1	The coil current
μ_0	H/m	$4\pi \times 10^{-7}$	The vacuum permeability

Table 2: Parameters of the PS.

Parameter	Unit	Value	Definition
h_u	mm	25	The height of the upper chamber
h_l	mm	35	The height of the lower chamber
A_u	mm^2	412.3	The cross-sectional area of the upper chamber
A_l	mm^2	490.9	The cross-sectional area of the lower chamber
λ	—	1.4	Gas variability index

the isolation system when the height of the upper chamber changes from 24 mm to 28 mm with an interval of 1 mm. Note that the total height of the upper and lower chambers is 60 mm. The height of the lower chamber, the pressure, and coil current of the QZS isolation system vary with the height of the upper chamber.

Figure 3 illustrates that as the height of the upper chamber decreases, the force-displacement curve and the stiffness-displacement curve of the isolation system are smoother, and the dynamic stiffness near the equilibrium position is smaller, so the isolation performance is better. The height of the upper chamber is set to 25 mm due to the limitation of the minimum pressure of the chamber and the maximum current of the coil. In addition, the advantage of the nonlinear stiffness of the isolation system can also be found in Figure 3. The dynamic stiffness of the system is close to 0 and almost unchanged when the displacement of the isolated object is small and within 5 mm near the equilibrium position, which can achieve superior low-frequency isolation performance. On the contrary, the system stiffness increases rapidly to ensure the support capacity of the isolator and avoid the risk of collision when the deviation from the equilibrium position is large.

3.3. Applicability of the QZS Isolation System for Variable Loads. The proposed isolator can adapt to variable loads by adjusting the pressure and coil current. It can be seen from Equation (10) that changing p_l, p_u, and i proportionally can maintain the QZS characteristics of the system when the load mg changes. Note that the adjustment process is to first adjust the pressure so that the working position of the isolation system remains unchanged, and then adjust the current to make the negative stiffness generated by the electromagnetic force match the positive stiffness, thereby maintaining the QZS characteristics of the system. For the proposed isolator, the adjustment process and method to deal with the increase and decrease of load are the same, so this article only discusses the situation that the load increases.

In order to analyze the influence of load changes on the static characteristics and dynamic response of the isolator more clearly, the parameter β is used to represent the multiple of the load increase. For the case of $m = 5kg$, $p_l = 0.204Mp_a$, $p_u = 0.124Mp_a$, and $i = 1.12A$, Figure 4 shows the change of the force-displacement characteristics and the stiffness curve of the QZS isolation system when the load mg increases $1 + \beta$ times. It can be found that as the load gradually grows, the balanced position of the system remains unchanged, and the stiffness of the system almost remains unchanged near the equilibrium position and increases slightly on both sides away from the balanced position. Therefore, it can be considered that the proposed QZS isolator can still maintain the working position and QZS characteristics under variable loads, which broadens the applied range of the isolator. Certainly, if the load changes sharply, the range of QZS of the isolator will be greatly reduced, which will lead to a decrease in isolation performance.

3.4. Approximation of Force-Displacement Characteristics of the Isolation System. The Taylor polynomial is used in this study to approximate the restoring force of the isolation system at $x = 0$ to simplify the calculation.

Figure 5 illustrates that the approximate restoring force and stiffness are relatively consistent with the accurate value near the equilibrium position, but the deviation is large on both sides. On the side of the equilibrium position, the error between the accurate value and the fifth-order Taylor polynomial is 1.9%, and the error between the accurate value and the seventh-order and ninth-order Taylor polynomials does not exceed 0.3%,

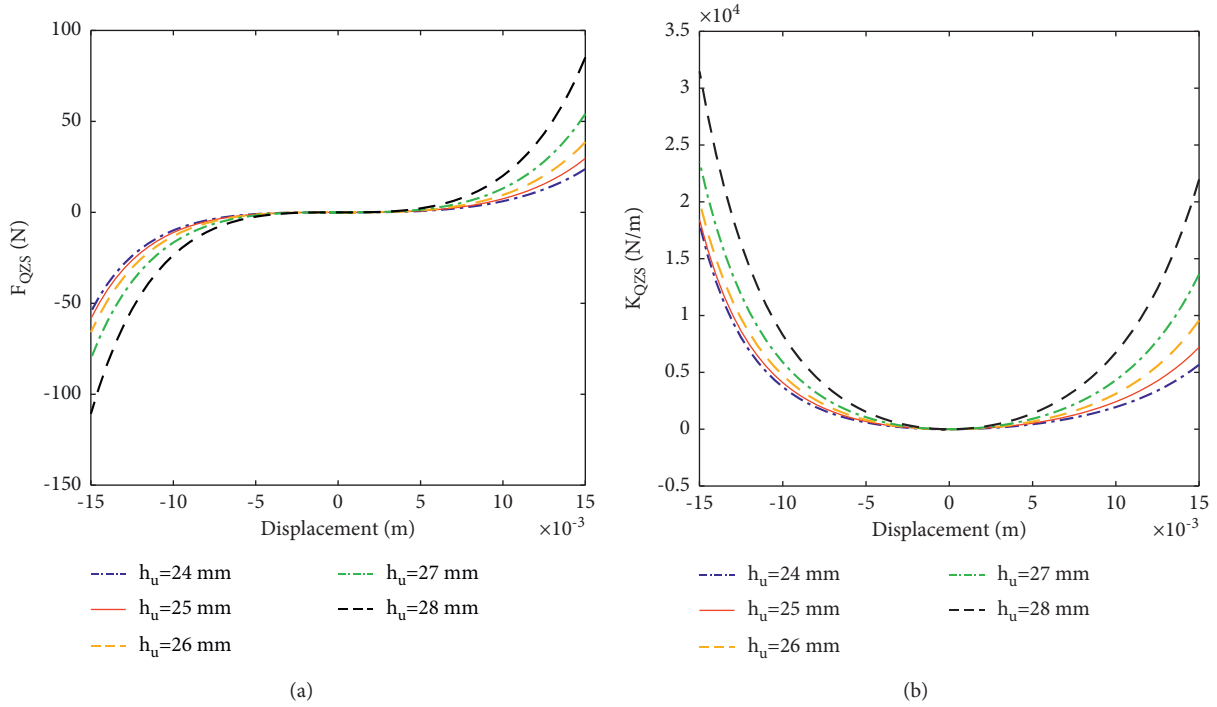

Figure 3: (a) The force-displacement curve under different h_u. (b) The stiffness-displacement curve under different h_u.

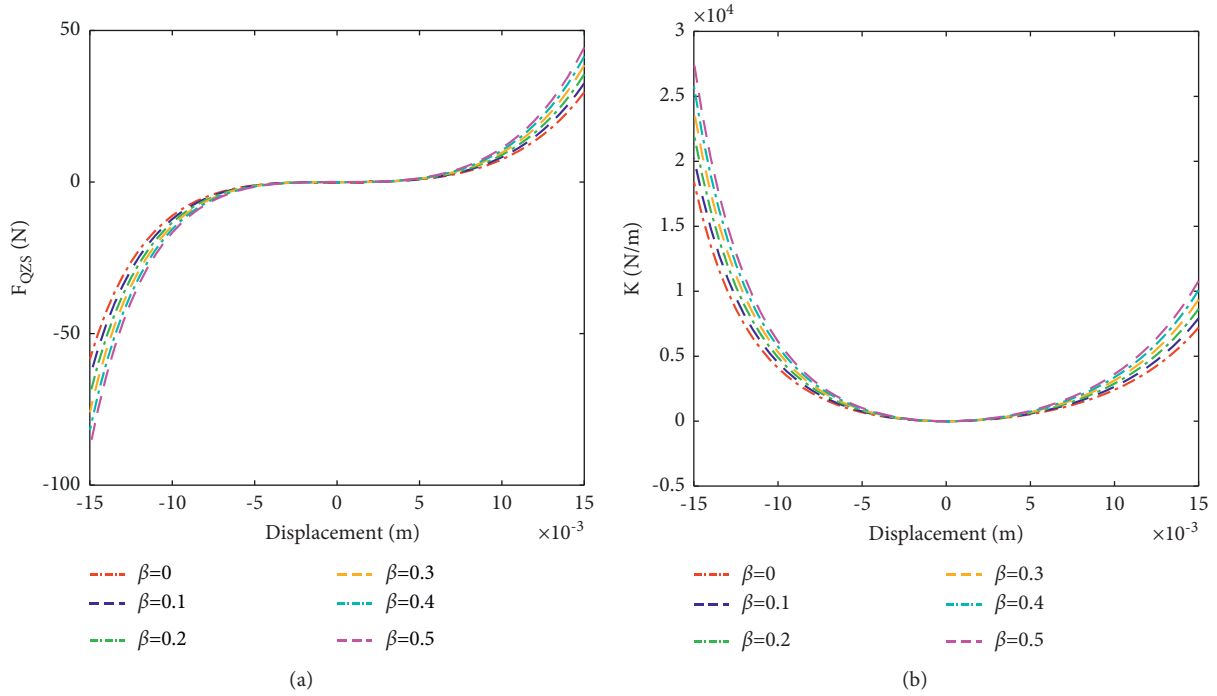

Figure 4: (a) The restoring force of the system under different β. (b) The stiffness of the system under different β.

as is shown in Figure 6. However, higher-order approximation leads to more complicated calculations and longer calculation time. Therefore, as a trade-off, a seventh-order Taylor polynomial is selected to approximate Equation (5), which can be written as

$$F = f_1 x + f_2 x^2 + f_3 x^3 + f_4 x^4 + f_5 x^5 + f_6 x^6 + f_7 x^7, \tag{11}$$

where f_1, f_2, f_3, f_4, f_5, f_6, and f_7 are Taylor polynomial coefficients.

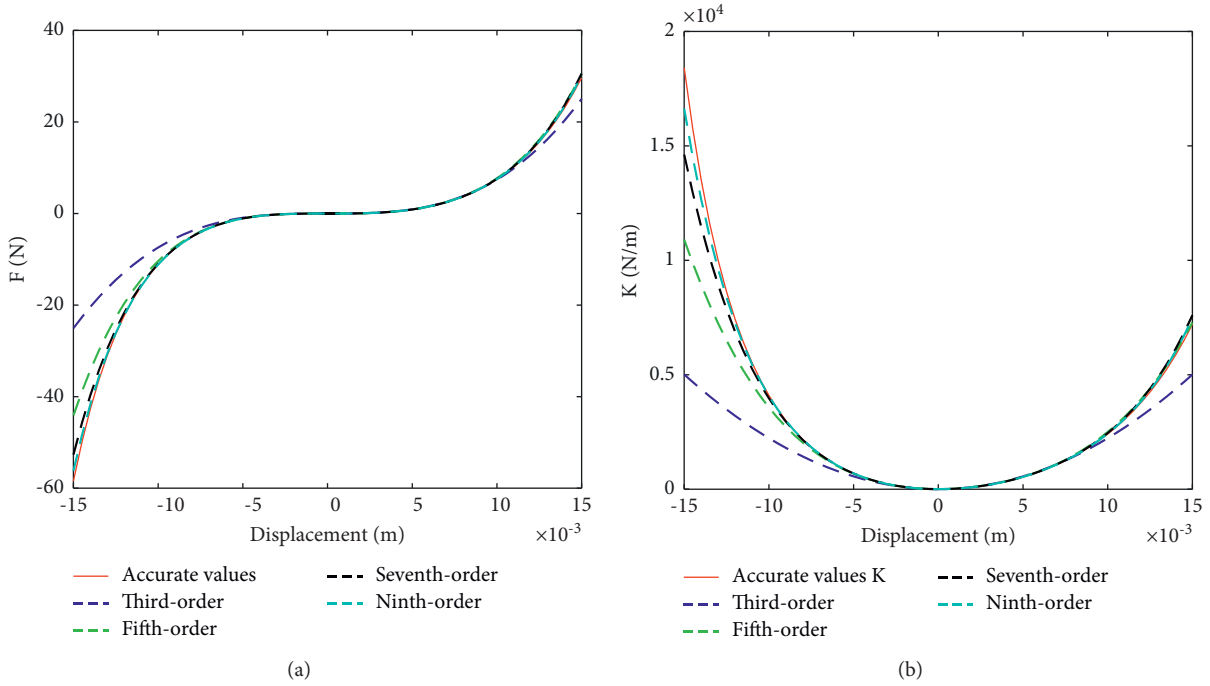

Figure 5: Taylor polynomial approximation: (a) approximation of the restoring force; (b) approximation of the stiffness.

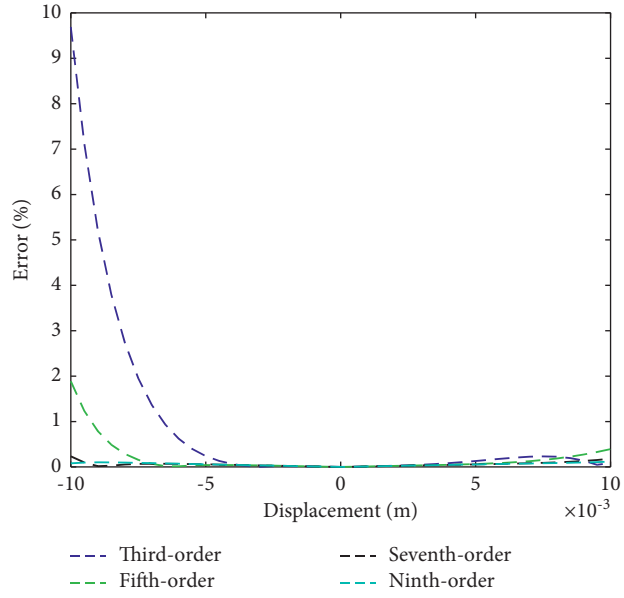

Figure 6: Approximate error.

4. Dynamic Response of the QZS Isolator

4.1. Amplitude-Frequency Response under Harmonic Excitation Force. The dynamic model of the QZS isolation system is equivalent to an SDOF system with stiffness K and damping c in the vertical direction as is shown in Figure 1(c). When the harmonic excitation force $F_e \cos(\omega t)$ (F_e and ω are the amplitude and frequency of the excitation force) is applied to the load at the balance position, and the restoring force of the isolation system adopts the approximate force of Equation (11), the equation of motion is given by

$$m\ddot{x} + c\dot{x} + F = F_e \cos(\omega t). \tag{12}$$

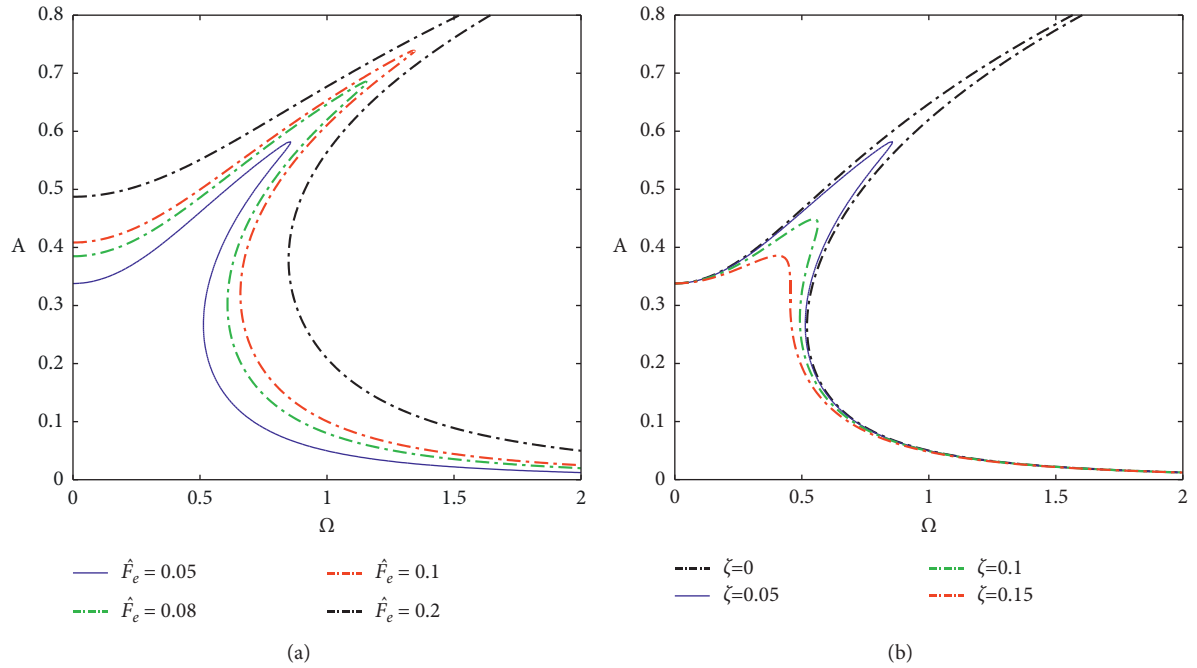

Figure 7: (a) Effect of excitation amplitude on the amplitude-frequency response ($\zeta = 0.05$). (b) Effect of damping ratio on the amplitude-frequency response ($\hat{F}_e = 0.05$).

Transforming Equation (12) dimensionless form, which can be written as

$$\ddot{\hat{x}} + 2\zeta\dot{\hat{x}} + \overline{f}_1\hat{x} + \overline{f}_2\hat{x}^2 + \overline{f}_3\hat{x}^3 + \overline{f}_4\hat{x}^4 + \overline{f}_5\hat{x}^5 + \overline{f}_6\hat{x}^6 + \overline{f}_7\hat{x}^7 = \hat{F}_e\cos(\Omega\tau), \tag{13}$$

where $\hat{x} = x/h_l$, $\omega_n = \sqrt{K/m}$, $\zeta = c/2m\omega_n$, $\hat{F} = F/Kh_l$, $\overline{f}_1 = f_1/K$, $\overline{f}_2 = f_2h_l/K$, $\overline{f}_3 = f_3{h_l}^2/K$, $\overline{f}_4 = f_4{h_l}^3/K$, $\overline{f}_5 = f_5{h_l}^4/K$, $\overline{f}_6 = f_6{h_l}^5/K$, $\overline{f}_7 = f_7{h_l}^6/K$, $\hat{F}_e = F_e/Kh_l$, $\Omega = \omega/\omega_n$, $\tau = \omega_n t$, $\dot{x} = dx/dt = h_l d\hat{x}/dt = \omega_n h_l d\hat{x}/d\tau = \omega_n h_l\dot{\hat{x}}$, and $\ddot{x} = d^2x/dt^2 = {\omega_n}^2 h_l d^2\hat{x}/d\tau^2 = {\omega_n}^2 h_l\ddot{\hat{x}}$.

The harmonic balance method (HBM) is applied to solve Equation (13), and the form of the system response is assumed as $\hat{x} = A\cos(\Omega\tau + \theta)$. The following equation can be obtained by making the coefficients of the $\cos\Omega\tau$ and $\sin\Omega\tau$ terms on both sides of Equation (13) equal after substituting $\hat{x} = A\cos(\Omega\tau + \theta)$ into Equation (13):

$$\begin{cases} -A\Omega^2 + \overline{f} = \hat{F}_e\cos\theta, \\ -2\zeta A\Omega = \hat{F}_e\sin\theta, \end{cases} \tag{14}$$

where $\overline{f} = \overline{f}_1 A + 3/4\overline{f}_3 A^3 + 5/8\overline{f}_5 A^5 + 35/64\overline{f}_7 A^7$.

Then the amplitude-frequency response equation of the isolation system can be derived as follows:

$$\left(-A\Omega^2 + \overline{f}\right)^2 + (-2\zeta A\Omega)^2 = {\hat{F}_e}^2. \tag{15}$$

Figure 7 shows the amplitude-frequency curves obtained from Equation (15) under different parameters. It can be observed from Figure 7(a) that as the excitation amplitude grows, the response amplitude curve shifts to the upper right as a whole, and the jump frequency increases. However, the effect of the damping ratio on the response amplitude curve is the opposite. As the damping ratio increases, the jump frequency of the system decreases or even disappears in Figure 7(b). Therefore, a small damping ratio or a large excitation amplitude will make the nonlinear behavior of the system response more apparent, which is detrimental to the isolation performance of the system.

The analytical solution of Equation (15) is obtained by the first-order harmonic approximation. The numerical analysis of Equation (13) is performed simultaneously to verify the efficiency of the analytical solution. The result of the comparison of the analytical solution and the numerical solution is shown in Figure 8. Note that the method used in the numerical analysis is the forward frequency sweep and the backward frequency sweep of the Runge–Kutta method. It can be observed from Figure 8 that the amplitude-frequency responses obtained by the Runge–Kutta method and HBM are consistent in the high-frequency area, and the solution of the numerical method is larger than that of the analytical method in the low-frequency area. This is because the response of the isolation system in the low-frequency area is more complex, including not only the first-order harmonic but also the high-order harmonics and even chaos.

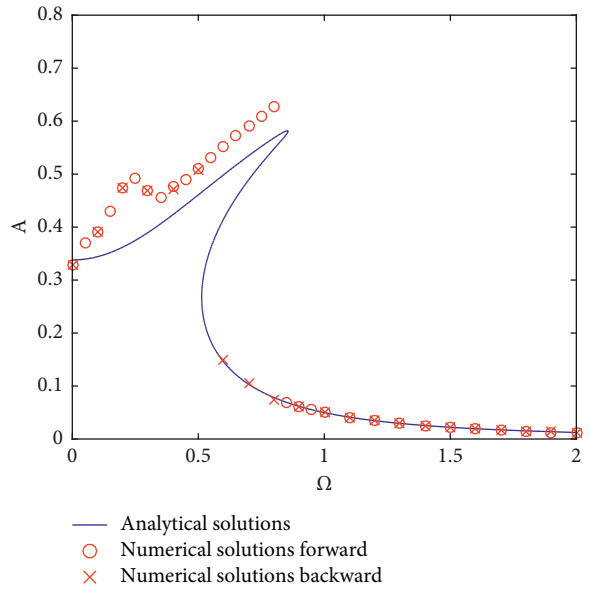

FIGURE 8: Analytical solutions and numerical solutions of the amplitude-frequency response ($\zeta = 0.05$, $\widehat{F}_e = 0.05$).

The complex components of the system response are revealed by studying the amplitude spectrum and phase trajectory diagram of the system response under different frequency ratios to further verify and explain the results shown in Figure 8, such as $\Omega_1 = 0.1$, $\Omega_2 = 0.4$, $\Omega_3 = 0.8$, and $\Omega_4 = 2$. Figures 9(a) and 9(b) illustrate the amplitude spectrum and the phase trajectory diagram of the isolation system response when $\Omega_1 = 0.1$. It can be observed that the amplitude spectrum includes not only the first-order harmonic but also a variety of super-harmonic components, and the phase trajectory diagram is complex. Therefore, the numerical solution is slightly different from the analytical solution. As shown in Figures 9(c)–9(f) when $\Omega_2 = 0.4$ and $\Omega_3 = 0.8$, the amplitude spectrum shows that the system response is mainly composed of the first-order harmonic and smaller second-order and third-order harmonics, and the phase trajectory diagram is a closed curve, which illustrates that the system has a single period motion. It can be found from Figures 9(g) and 9(h) that the system response only includes the first-order harmonic when $\Omega_4 = 2$, and the results obtained by the Runge–Kutta method and HBM are consistent. Although there is a deviation between the analytical solution and the numerical solution in the low-frequency area and the ultra-low-frequency area, the jump phenomenon of amplitude-frequency response can be observed through the analytical solution, and the unstable solution of the system can also be obtained.

4.2. Force Transmissibility. The force transmissibility (FT) of the isolator is defined as the amplitude ratio of the force transferred to the base to the excitation force and is an important index to evaluate the ability of the isolator to reduce the interference of the external dynamic load. According to the dynamic model, the force transferred to the base is given by

$$\widehat{f}_j = 2\zeta\dot{\widehat{x}} + \overline{f}_1\widehat{x} + \overline{f}_2\widehat{x}^2 + \overline{f}_3\widehat{x}^3 + \overline{f}_4\widehat{x}^4 + \overline{f}_5\widehat{x}^5 + \overline{f}_6\widehat{x}^6 + \overline{f}_7\widehat{x}^7. \tag{16}$$

The amplitude of $\widehat{f}_j$ can be obtained by substituting $\widehat{x} = A\cos(\Omega\tau + \theta)$ into Equation (16) as follows:

$$\widehat{F}_j = \sqrt{(2\zeta A\Omega)^2 + \overline{f}^2}. \tag{17}$$

The FT of the QZS isolation system in the form of the decibel is as follows:

$$T_f = 20\lg\left(\frac{\sqrt{(2\zeta A\Omega)^2 + \overline{f}^2}}{\widehat{F}_e}\right). \tag{18}$$

The numerical analysis is implemented to verify the analytical result of Equation (18). Now the FT of the isolation system is redefined as the energy transmissibility; that is, the ratio between the root mean square (RMS) of the energy transferred to the base and that of the excitation energy in a period is given by

$$T_e = 20\lg\left(\frac{\sqrt{\Omega/2\pi\int_0^{2\pi/\Omega}\widehat{f}_j{}^2 d\tau}}{\sqrt{\Omega/2\pi\int_0^{2\pi/\Omega}\left(\widehat{F}_e\cos(\Omega\tau)\right)^2 d\tau}}\right), \tag{19}$$

Figure 10 shows the numerical and analytical solutions of the FT. It can be observed that the numerical solution and the analytical solution are in good agreement, and the jump frequency of the analytical solution is also verified. However, the numerical solution is slightly larger than the analytical solution in the low-frequency area, which is caused by the complexity of the response.

The initial isolation frequency and peak FT of the linear system and QZS system in Figure 10 are $\sqrt{2}\omega_n$, 20.04 dB and $0.856\omega_n$, 18.68 dB, respectively. Therefore, this also shows that the linear system only works in the range of more than $\sqrt{2}$ times the natural frequency of the system, and the QZS system can achieve better isolation performance as long as the external frequency is greater than the jumping frequency. In addition, the FT of the QZS system is smaller than that of the linear system in the high-frequency area. Therefore, it can be considered that the proposed QZS system has a lower initial isolation frequency and better isolation performance than the linear system.

4.3. Force Transmissibility under Variable Loads. The system can obtain QZS characteristics and superior low-frequency isolation performance by choosing the appropriate pressure and coil current when the load is mg. Once the load increases $1 + \beta$ times, the existing QZS isolator cannot take effective measures to cope with the situation, which will lead to poor isolation performance. For the proposed QZS isolator, the deviation of the new stable position from the working position is x_0 when the load increases, and the equilibrium equation of the isolation system can be written as

$$m\ddot{x} + c\dot{x} + F(x + x_0) = F_e\cos(\omega t) + \beta mg. \tag{20}$$

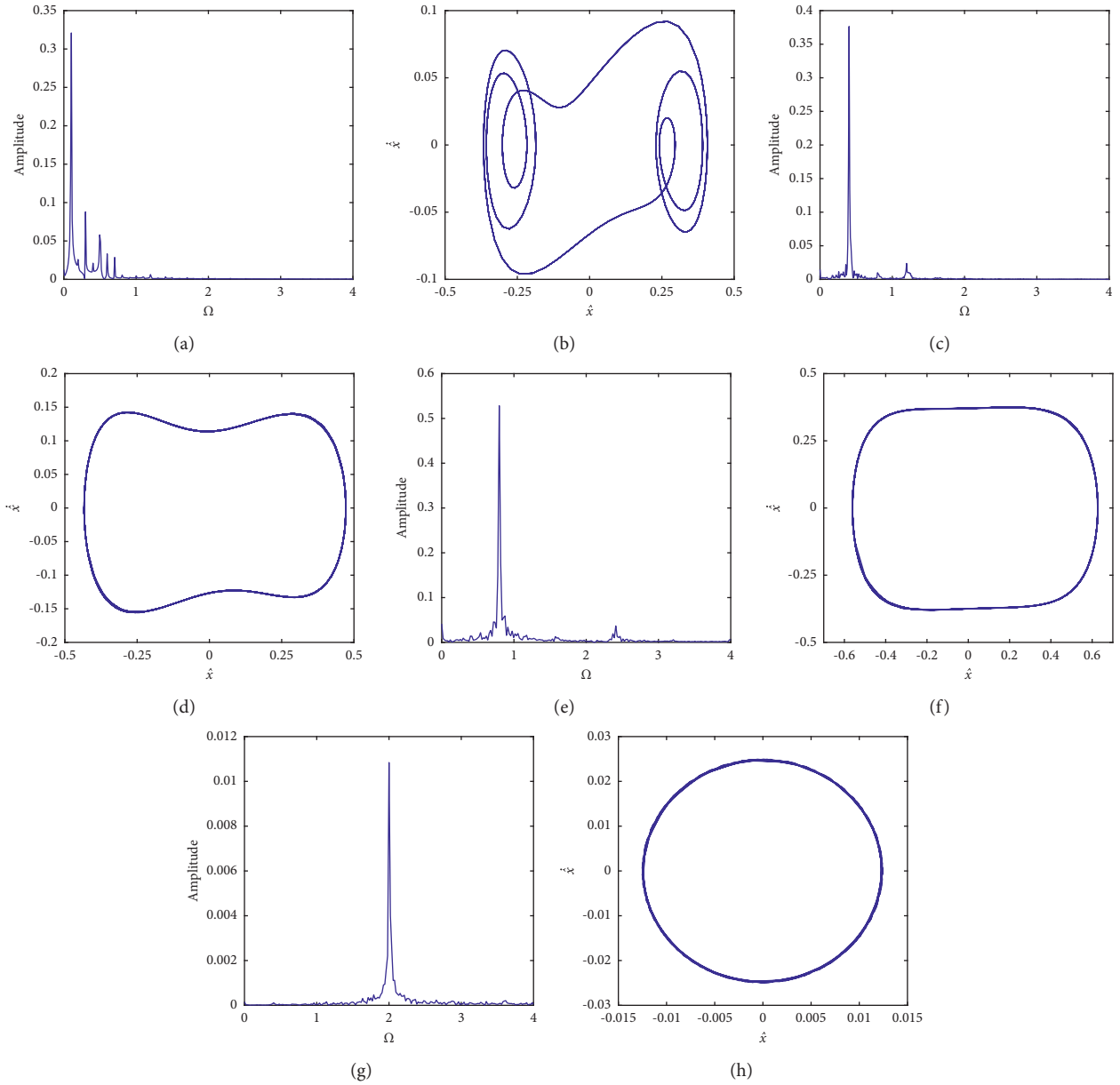

Figure 9: Amplitude spectrum and phase trajectory diagram of the isolation system response. (a, b) When $\Omega_1 = 0.1$; (c, d) when $\Omega_2 = 0.4$; (e, f) when $\Omega_3 = 0.8$; and (g, h) when $\Omega_4 = 2$.

Select the previous parameters to compare the isolation performance of the proposed QZS isolator under different loads. Figure 11 shows that the increase of load causes the FT curve of the isolation system to move to the right, which shortens the isolation frequency band and reduces the low-frequency isolation performance. The reason is that the new balance position of the isolation system deviates from the set working position due to the change of load, which leads to the increase in the dynamic stiffness of the system. The QZS isolator will no longer have the advantage of low-frequency vibration isolation when the deviation is large.

Figure 12 shows the FT of the QZS isolation system after adjusting the pressure and coil current. The peak FT increases slightly and the FT curve shifts slightly to the right in the jump frequency range when the load increases, while the FT remains unchanged in other frequency ranges. Thus, the conclusion can be drawn that the FT of the isolation system remains unchanged. The isolation system still maintains superior low-frequency isolation performance under different loads, which is difficult to achieve for most QZS isolators.

4.4. Displacement Transmissibility under Variable Loads. The analytical expression of the displacement transmissibility (DT) of the QZS isolator is derived to evaluate the ability of the isolator to reduce the vibration interference from the base when the load changes. As is shown in

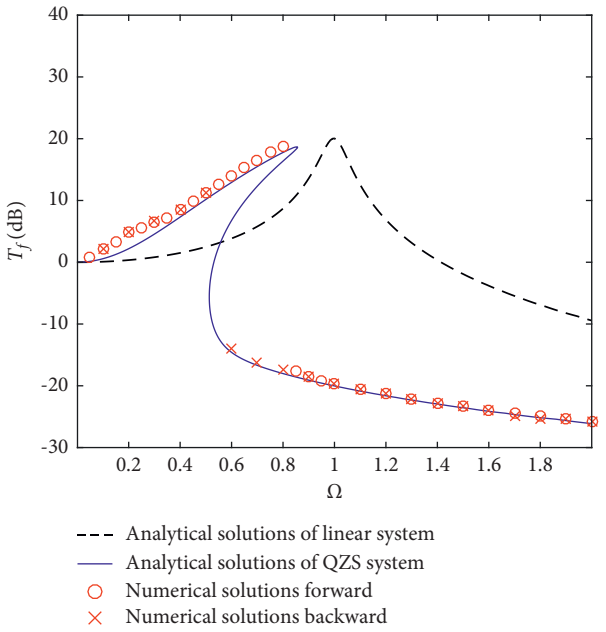

Figure 10: The force transmissibility of the QZS system and the linear system ($\zeta = 0.05$, $\widehat{F}_e = 0.05$).

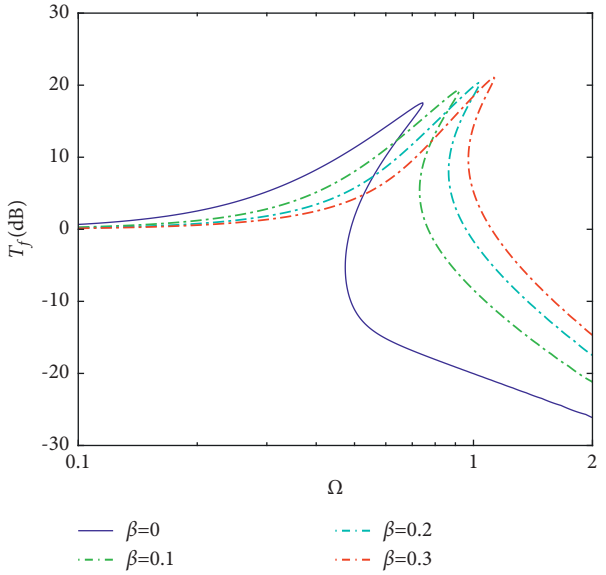

Figure 11: The force transmissibility of the QZS isolation system under different β ($\zeta = 0.05$, $\widehat{F}_e = 0.05$).

Figure 1(c), the absolute displacement of the isolated object in the vertical direction is y when the excitation displacement $x_j = \widehat{X}_j \cos(\omega t)$ is applied to the base. Then the dynamic equation of the isolation system is given by

$$m\ddot{u} + c\dot{u} + f_1 u + f_2 u^2 + f_3 u^3 + f_4 u^4 + f_5 u^5 + f_6 u^6 + f_7 u^7 = -m\ddot{x}_j, \tag{21}$$

where $u = y - x_j$ is the relative displacement of the isolated object.

Transforming Equation (21) dimensionless form, which can be written as

$$\ddot{\widehat{u}} + 2\zeta\dot{\widehat{u}} + \overline{f}_1\widehat{u} + \overline{f}_2\widehat{u}^2 + \overline{f}_3\widehat{u}^3 + \overline{f}_4\widehat{u}^4 + \overline{f}_5\widehat{u}^5 + \overline{f}_6\widehat{u}^6 + \overline{f}_7\widehat{u}^7 = \widehat{X}_j\Omega^2\cos(\Omega\tau), \tag{22}$$

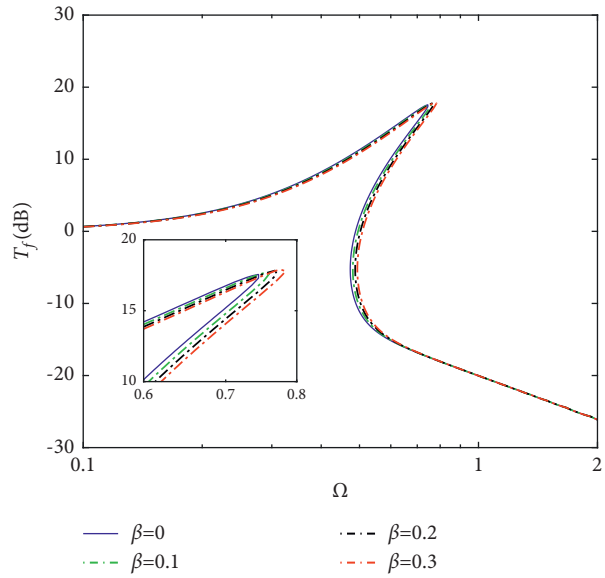

Figure 12: The force transmissibility of the QZS isolation system after adjusting the pressure and coil current ($\zeta = 0.05$, $\widehat{F}_e = 0.05$).

where $\widehat{u} = u/h_l$ and $\widehat{X}_j = X_j/h_l$. Other parameters involved in Equation (22) are the same as those in Equation (13).

The form of the response solution is assumed as follows:

$$\widehat{u} = A\cos(\Omega\tau + \theta). \tag{23}$$

The following equation can be obtained after substituting Equation (23) into Equation (22):

$$\begin{cases} -A\Omega^2 + \overline{f} = \widehat{X}_j\Omega^2\cos\theta, \\ -2\zeta A\Omega = \widehat{X}_j\Omega^2\sin\theta. \end{cases} \tag{24}$$

Then the amplitude-frequency response equation of the system is written as follows:

$$\left(-A\Omega^2 + \overline{f}\right)^2 + (-2\zeta A\Omega)^2 = \left(\widehat{X}_j\Omega^2\right)^2. \tag{25}$$

The absolute DT of the isolation system is defined as the ratio of the absolute displacement of the isolated object to the excitation displacement, which can be expressed in decibels as follows:

$$T_d = 20\lg\left(\frac{|x|}{|x_j|}\right) = 20\lg\left(\frac{|u + x_j|}{|x_j|}\right) = 10\lg\left(\frac{A^2 + \widehat{X}_j^2 + 2\widehat{X}_j A\cos\theta}{\widehat{X}_j^2}\right). \tag{26}$$

The deviation of the new stable position from the working position is u_0 when the load increases, and the equilibrium equation of the isolation system can be written as

$$m\ddot{u} + c\dot{u} + F(u + u_0) = -m\ddot{x}_j + \beta mg. \tag{27}$$

Figure 13 shows the DT of the system without taking any measures when the load increases $1 + \beta$ times. Note that the isolation system has the effect of isolation only when $T_d < 0$. It can be observed from Figure 13 that the DT curve of the system bends to the right and the peak transmissibility is large when $\zeta = 0.05$ and $\widehat{X}_j = 0.1$. This is due to the nonlinearity of the isolator, which can be reduced or eliminated by increasing the damping ratio. As the load increases, the DT curve changes significantly, which is manifested as the curve moves to the right by a large margin and the initial isolation frequency increases, and the ability of the isolator to reduce the vibration interference from the base drops greatly. Similar to the change of FT under different loads, this is caused by the increase in the dynamic stiffness of the system as the load increases. The problem of the decrease of the isolation performance due to variable loads is common and difficult to solve for most QZS isolators.

The proposed QZS isolator can reduce the damage caused by variable loads by changing the positive and negative stiffness. The DT curve after adjusting the coil current and pressure is shown in Figure 14. It can be found that the jump frequency of DT increases slightly when the load increases, which shortens the isolation frequency band slightly. However, the curve remains almost unchanged in other frequency ranges. This is because the proportional change of pressure and coil current keeps the working position and QZS characteristics of the isolator unchanged.

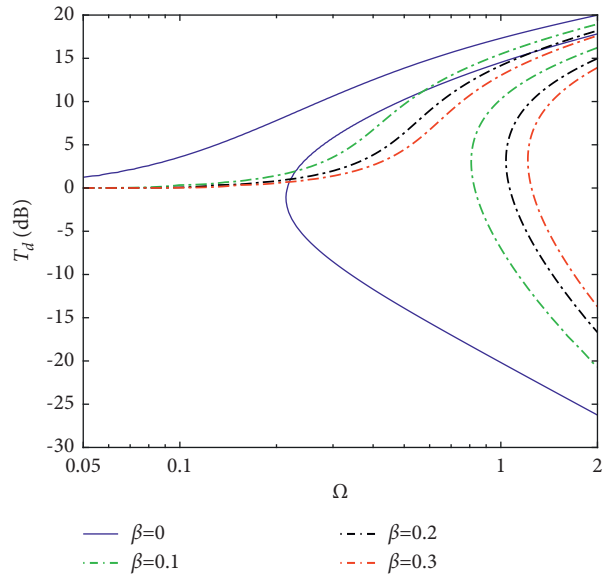

Figure 13: The displacement transmissibility of the QZS isolation system under different β ($\zeta = 0.05$, $\widehat{X}_j = 0.1$).

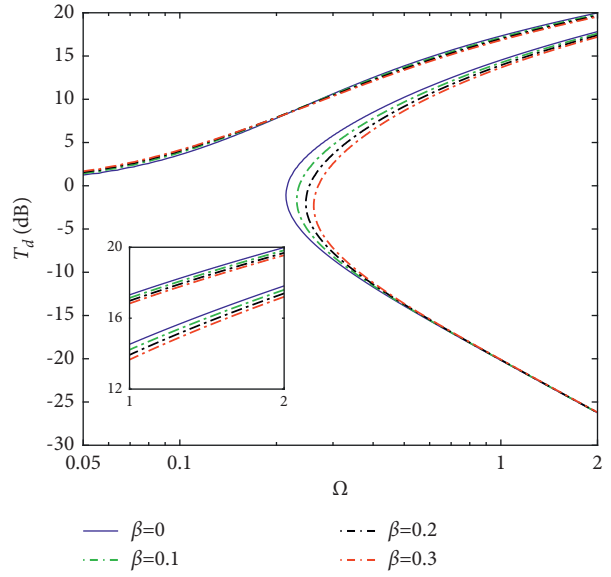

Figure 14: The displacement transmissibility of the QZS isolation system after adjusting the pressure and coil current ($\zeta = 0.05$, $\widehat{X}_j = 0.1$).

Although the increase in the load will still change the isolation performance, this change is small or even negligible compared to the change of the isolation performance before the measures are taken. Therefore, it can be concluded that the isolation performance of the proposed QZS isolator remains almost unchanged under variable loads.

5. Time-Domain Simulation of the Isolation System

The response displacement of the load is simulated in the time domain to evaluate the isolation performance of the isolation system when the harmonic excitation displacement $\widehat{X}_j \cos(\Omega\tau)$ is applied to the base.

Figure 15 shows the dimensionless response displacement of the load when $\widehat{X}_j = 0.1$ and $\Omega = 1, 2$. For $\Omega = 1$, the RMS of the load response displacement is 4.66 times the RMS of the excitation displacement when there is no current in the coil, and it decreases rapidly to 10.01% once the coil is excited by the current of 1.12 A. For $\Omega = 2$, the RMS of the load response displacement decreases from 35.01% of the RMS of the excitation displacement to 5.39% after the coil is excited by the current of 1.12 A. The change of the response displacement of the system indicates that the dynamic stiffness near the balance position of the system decreases to close to 0 and the natural frequency decreases after the coil current is applied, which improves the isolation performance.

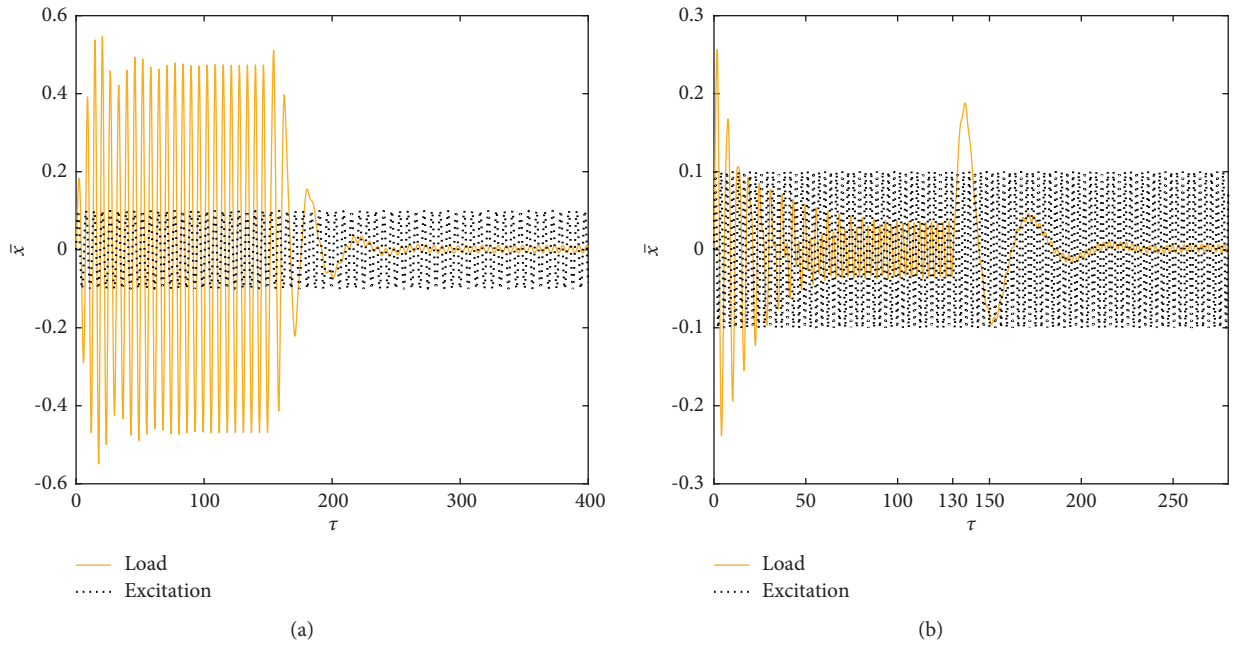

Figure 15: The dimensionless response displacement under different Ω: (a) $\Omega = 1$, the coil current is applied when $\tau = 150$; (b) $\Omega = 2$, the coil current is applied when $\tau = 130$.

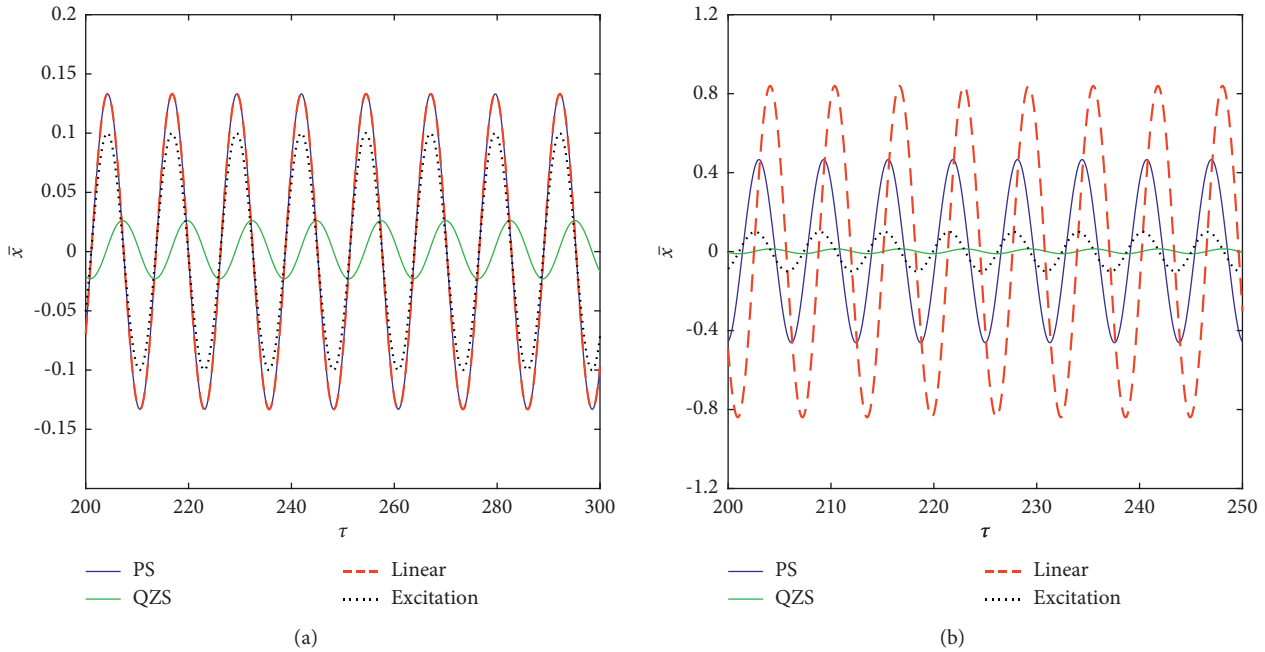

Figure 16: Continued.

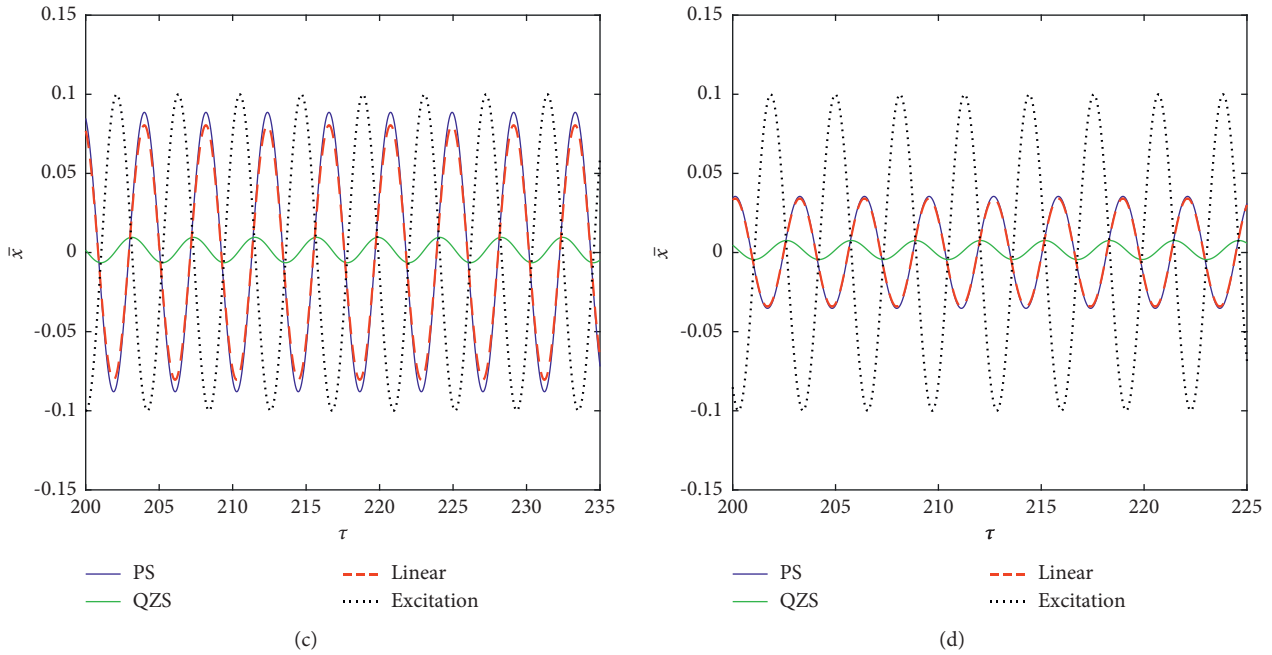

Figure 16: Dimensionless response displacement of different systems under different Ω: (a) Ω = 0.5; (b) Ω = 1; (c) Ω = 1.5; and (d) Ω = 2.

Figure 16 shows the response displacements of the PS isolation system, the proposed QZS isolation system, and the linear isolation system when $\widehat{X}_j = 0.1$ and Ω = 0.5, 1, 1.5, 2. The response displacement of the PS system is almost the same as that of the linear system. However, the response displacement of the PS system is smaller due to the nonlinear characteristics of the PS when Ω = 1.

For Ω = 0.5, the proposed QZS system has already exerted the isolation effect, and the RMS of the load response displacement is 24.74% of that of the excitation displacement. However, the RMS of the load response displacement of the PS system and the linear system is 133% of that of the excitation displacement. It can be observed from Figure 16 that the proposed QZS isolation system always maintains better isolation performance, which appears as a smaller response amplitude and a lower isolation frequency.

6. Conclusion

This paper proposes a design of the QZS isolator that can adapt to different loads with parallel ES and PS. The restoring force of the isolation system is derived, and three decisive parameters for realizing QZS characteristics are obtained. The adjustment method to adapt to variable loads is given. The restoring force of the isolation system is approximated by the seventh-order Taylor polynomial and the HBM is applied for the dynamic analysis of the system. Theoretical research shows that as the load increases, the FT and DT raise and the isolation performance decreases rapidly without taking any measures. However, changing the pressure and coil current in the same proportion to maintain the working position and QZS characteristics of the system can lessen the application limits of the isolator. The time-domain simulation results show that the system response displacement decreases greatly when the coil winding is excited by the current, and the proposed isolator has apparent advantages in response amplitude and isolation frequency band over the linear system and PS. Verifying the ability to adapt to variable loads of the isolator through experiments is a crucial work in the future. A control strategy of adjusting the current is also needed in the following work, which can enhance the accuracy of the adjustment results and ensure that the isolator reaches the QZS state.

Appendix

Here, the specific expression of the electromagnetic force calculated by the filament method is given. The attractive forces produced by the ring magnet and the upper and lower energized coil windings are as follows:

$$
\begin{aligned}
F_{CM} &= \sum_{j=1}^{N_{RC}} \sum_{q=1}^{N_{HM}} \sum_{s=1}^{N_{HC}} \frac{\mu_0 i_1 i_2 z_C(qs) k_{1C}}{4\sqrt{R_{1M} r(j)}} \left[2K(k_{1C}) - \frac{2 - {k_{1C}}^2}{1 - {k_{1C}}^2} E(k_{1C}) \right] \\
&\quad - \sum_{j=1}^{N_{RC}} \sum_{q=1}^{N_{HM}} \sum_{s=1}^{N_{HC}} \frac{\mu_0 i_1 i_2 z_C(qs) k_{2C}}{4\sqrt{R_{2M} r(j)}} \left[2K(k_{2C}) - \frac{2 - {k_{2C}}^2}{1 - {k_{2C}}^2} E(k_{2C}) \right], \\
F_{DM} &= \sum_{j=1}^{N_{RC}} \sum_{q=1}^{N_{HM}} \sum_{s=1}^{N_{HC}} \frac{\mu_0 i_1 i_2 z_{\ D}(qs) k_{2\ D}}{4\sqrt{R_{2M} r(j)}} \left[2K(k_{2\ D}) - \frac{2 - {k_{2\ D}}^2}{1 - {k_{2\ D}}^2} E(k_{2\ D}) \right] \\
&\quad - \sum_{j=1}^{N_{RC}} \sum_{q=1}^{N_{HM}} \sum_{s=1}^{N_{HC}} \frac{\mu_0 i_1 i_2 z_{\ D}(qs) k_{1\ D}}{4\sqrt{R_{1M} r(j)}} \left[2K(k_{1\ D}) - \frac{2 - {k_{1\ D}}^2}{1 - {k_{1\ D}}^2} E(k_{1\ D}) \right],
\end{aligned}
\tag{A.1}
$$

where

$$
\begin{aligned}
& i_1 = \frac{JH_M}{\mu_0 N_{HM}}, i_2 = \frac{Ni(C)}{N_{RC} \times N_{HC}}, r(j) = R_{1C} + \left(\frac{j}{2}\right)\left(\frac{R_{2C} - R_{1C}}{N_{RC}}\right), \\
& z_C(qs) = z + \left(\frac{q}{2}\right)\left(\frac{H_M}{N_{HM}}\right) + \left(\frac{s}{2}\right)\left(\frac{H_C}{N_{HC}}\right), z_{\ D}(qs) = 30 - z + \left(\frac{q}{2}\right)\left(\frac{H_M}{N_{HM}}\right) + \left(\frac{s}{2}\right)\left(\frac{H_C}{N_{HC}}\right), \\
& k_{1C} = \sqrt{\frac{4R_{1M} r(j)}{[R_{1M} + r(j)]^2 + z_C(qs)^2}}, k_{2C} = \sqrt{\frac{4R_{2M} r(j)}{[R_{2M} + r(j)]^2 + z_C(qs)^2}}, \\
& k_{1\ D} = \sqrt{\frac{4R_{1M} r(j)}{[R_{1M} + r(j)]^2 + z_{\ D}(qs)^2}}, k_{2\ D} = \sqrt{\frac{4R_{2M} r(j)}{[R_{2M} + r(j)]^2 + z_{\ D}(qs)^2}}, \\
& K(k) = \int_0^{\frac{\pi}{2}} \frac{d\theta}{\sqrt{\left(1 - k^2 \sin^2 \theta\right)}}, E(k) = \int_0^{\frac{\pi}{2}} \sqrt{\left(1 - k^2 \sin^2 \theta\right)} d\theta.
\end{aligned}
\tag{A.2}
$$

Among them, j is the jth turn in the radial direction of the coil winding, q is the qth turn in the axial direction of the ring magnet, and s is the sth turn in the axial direction of the coil winding.

Data Availability

All data generated or analyzed during this study are included in this article.

Conflicts of Interest

The authors declare that there are no conflicts of interest regarding the publication of this paper.

References

[1] R. Ma, K. Bi, and H. Hao, "Inerter-based structural vibration control: a state-of-the-art review," *Engineering Structures*, vol. 243, p. 112655, 2021.

[2] Y. Nakamura, A. Fukukita, K. Tamura et al., "Seismic response control using electromagnetic inertial mass dampers," *Earthquake Engineering & Structural Dynamics*, vol. 43, no. 4, pp. 507–527, 2014.

[3] H. Wang, W. Shen, Y. Li, H. Zhu, and S. Zhu, "Dynamic behavior and seismic performance of base-isolated structures with electromagnetic inertial mass dampers: analytical solutions and simulations," *Engineering Structures*, vol. 246, p. 113072, 2021.

[4] D. Pietrosanti, M. De Angelis, and A. Giaralis, "Experimental study and numerical modeling of nonlinear dynamic response of SDOF system equipped with tuned mass damper inerter (TMDI) tested on shaking table under harmonic excitation," *International Journal of Mechanical Sciences*, vol. 184, p. 105762, 2020.

[5] X. Shi and S. Zhu, "A comparative study of vibration isolation performance using negative stiffness and inerter dampers," *Journal of the Franklin Institute*, vol. 356, no. 14, pp. 7922–7946, 2019.

[6] H. S. Bouna, B. R. N. Nbendjo, and P. Woafo, "Isolation performance of a quasi-zero stiffness isolator in vibration isolation of a multi-span continuous beam bridge under pier base vibrating excitation," *Nonlinear Dynamics*, vol. 100, no. 2, pp. 1125–1141, 2020.

[7] A. Carrella, M. I. Friswell, A. Zotov, D. J. Ewins, and A. Tichonov, "Using nonlinear springs to reduce the whirling of a rotating shaft," *Mechanical Systems and Signal Processing*, vol. 23, no. 7, pp. 2228–2235, 2009.

[8] A. Carrella, M. J. Brennan, T. P. Waters, and V. Lopes, "Force and displacement transmissibility of a nonlinear isolator with high-static-low-dynamic-stiffness," *International Journal of Mechanical Sciences*, vol. 55, no. 1, pp. 22–29, 2012.

[9] C. Liu, K. Yu, and J. Tang, "New insights into the damping characteristics of a typical quasi-zero-stiffness vibration isolator," *International Journal of Non-linear Mechanics*, vol. 124, p. 103511, 2020.

[10] T. Deng, G. Wen, H. Ding, Z.-Q. Lu, and L.-Q. Chen, "A bio-inspired isolator based on characteristics of quasi-zero stiffness and bird multi-layer neck," *Mechanical Systems and Signal Processing*, vol. 145, p. 106967, 2020.

[11] G. Gatti, "Statics and dynamics of a nonlinear oscillator with quasi-zero stiffness behaviour for large deflections," *Communications in Nonlinear Science and Numerical Simulation*, vol. 83, p. 105143, 2020.

[12] F. Zhao, J. Ji, K. Ye, and Q. Luo, "An innovative quasi-zero stiffness isolator with three pairs of oblique springs," *International Journal of Mechanical Sciences*, vol. 192, p. 106093, 2021.

[13] K. Ye, J. C. Ji, and T. Brown, "Design of a quasi-zero stiffness isolation system for supporting different loads," *Journal of Sound and Vibration*, vol. 471, p. 115198, 2020.

[14] J. Zhou, X. Wang, D. Xu, and S. Bishop, "Nonlinear dynamic characteristics of a quasi-zero stiffness vibration isolator with cam-roller-spring mechanisms," *Journal of Sound and Vibration*, vol. 346, pp. 53–69, 2015.

[15] H. Junshu, M. Lingshuai, S. Jinggong, and Z. Peng, "Design and characteristics analysis of a nonlinear isolator using a curved-mount-spring-roller mechanism as negative stiffness element," *Mathematical Problems in Engineering*, vol. 2018, pp. 1–15, 2018.

[16] Y. Wang, H.-X. Li, C. Cheng, H. Ding, and L.-Q. Chen, "A nonlinear stiffness and nonlinear inertial vibration isolator," *Journal of Vibration and Control*, vol. 27, no. 11-12, pp. 1336–1352, 2021.

[17] Y. Wang, H. X. Li, C. Cheng, H. Ding, and L. Q. Chen, "Dynamic performance analysis of a mixed-connected inerter-based quasi-zero stiffness vibration isolator," *Structural Control and Health Monitoring*, vol. 27, no. 10, 2020.

[18] F. Zhang, M. Xu, S. Shao, and S. Xie, "A new high-static-low-dynamic stiffness vibration isolator based on magnetic negative stiffness mechanism employing variable reluctance stress," *Journal of Sound and Vibration*, vol. 476, p. 115322, 2020.

[19] C. Liu, R. Zhao, K. Yu, and B. Liao, "In-plane quasi-zero-stiffness vibration isolator using magnetic interaction and cables: theoretical and experimental study," *Applied Mathematical Modelling*, vol. 96, pp. 497–522, 2021.

[20] G. Dong, X. Zhang, S. Xie, B. Yan, and Y. Luo, "Simulated and experimental studies on a high-static-low-dynamic stiffness isolator using magnetic negative stiffness spring," *Mechanical Systems and Signal Processing*, vol. 86, pp. 188–203, 2017.

[21] X. Sun, F. Wang, and J. Xu, "Analysis, design and experiment of continuous isolation structure with Local Quasi-Zero-Stiffness property by magnetic interaction," *International Journal of Non-linear Mechanics*, vol. 116, pp. 289–301, 2019.

[22] K. Wang, J. Zhou, H. Ouyang, L. Cheng, and D. Xu, "A semi-active metamaterial beam with electromagnetic quasi-zero-stiffness resonators for ultralow-frequency band gap tuning," *International Journal of Mechanical Sciences*, vol. 176, p. 105548, 2020.

[23] Z.-Q. Lu, D. Wu, H. Ding, and L.-Q. Chen, "Vibration isolation and energy harvesting integrated in a Stewart platform with high static and low dynamic stiffness," *Applied Mathematical Modelling*, vol. 89, pp. 249–267, 2021.

[24] N. Zhou and K. Liu, "A tunable high-static-low-dynamic stiffness vibration isolator," *Journal of Sound and Vibration*, vol. 329, no. 9, pp. 1254–1273, 2010.

[25] J. Zhao, Y. Sun, J. Li et al., "A novel electromagnet-based absolute displacement sensor with approximately linear quasi-zero-stiffness," *International Journal of Mechanical Sciences*, vol. 181, p. 105695, 2020.

[26] S. Liu, P. Su, J. Wu, and Y. Fang, "A study of a nonlinear magnetic vibration isolator with quasi-zero-stiffness," *Journal of Vibroengineering*, vol. 20, no. 1, pp. 310–320, 2018.

[27] S. Yuan, Y. Sun, J. Zhao et al., "A tunable quasi-zero stiffness isolator based on a linear electromagnetic spring," *Journal of Sound and Vibration*, vol. 482, p. 115449, 2020.

[28] H. Pu, S. Yuan, Y. Peng et al., "Multi-layer electromagnetic spring with tunable negative stiffness for semi-active vibration isolation," *Mechanical Systems and Signal Processing*, vol. 121, pp. 942–960, 2019.

[29] Y. Jiang, C. Song, C. Ding, and B. Xu, "Design of magnetic-air hybrid quasi-zero stiffness vibration isolation system," *Journal of Sound and Vibration*, vol. 477, p. 115346, 2020.

[30] Z.-Q. Lu, D.-H. Gu, H. Ding, W. Lacarbonara, and L.-Q. Chen, "Nonlinear vibration isolation via a circular ring," *Mechanical Systems and Signal Processing*, vol. 136, p. 106490, 2020.

[31] L. Meng, J. Sun, W. Wu, and K. V. Singh, "Theoretical design and characteristics analysis of a quasi-zero stiffness isolator using a disk spring as negative stiffness element," *Shock and Vibration*, vol. 2015, pp. 1–19, 2015.

[32] Y. Ma, M. He, W. Shen, and G. Ren, "A planar shock isolation system with high-static-low-dynamic-stiffness characteristic based on cables," *Journal of Sound and Vibration*, vol. 358, pp. 267–284, 2015.

[33] X. Huang, Y. Chen, H. Hua, X. Liu, and Z. Zhang, "Shock isolation performance of a nonlinear isolator using Euler buckled beam as negative stiffness corrector: theoretical and experimental study," *Journal of Sound and Vibration*, vol. 345, pp. 178–196, 2015.

[34] J. Bian and X. Jing, "Analysis and design of a novel and compact X-structured vibration isolation mount (X-Mount) with wider quasi-zero-stiffness range," *Nonlinear Dynamics*, vol. 101, no. 4, pp. 2195–2222, 2020.

[35] A. Shiri and A. Shoulaie, "A new methodology for magnetic force calculations between planar spiral coils," *Progress In Electromagnetics Research*, vol. 95, pp. 39–57, 2009.